Journal of The Electrochemical Society, **151** (1) A151-A157 (2004)
0013-4651/2003/151(1)/A151/7/$7.00 © The Electrochemical Society, Inc.

Synthesis, Characterization, and Electrochemical Properties of Nanocrystalline Silver Thin Films Obtained by Spray Pyrolysis

J. Morales,[a,*] L. Sánchez,[a,z] F. Martín,[b] J. R. Ramos-Barrado,[b,*] and M. Sánchez[b]

[a]*Departamento de Química Inorgánica e Ingeniería Química, Facultad de Ciencias, Universidad de Córdoba, 14071 Córdoba, Spain*
[b]*Laboratorio de Materiales y Superficie (Unidad Asociada al Consejo Superior de Investigaciones Cientificas), Universidad de Málaga, Málaga, Spain*

Silver thin films were prepared using a spray pyrolysis method, silver acetate as the precursor, and stainless steel, heated at 225 and 300°C, as the substrate. Structural and morphological analyses carried out using X-ray diffraction, X-ray photoelectron spectroscopy (XPS), and scanning electron microscopy methods revealed the formation of highly homogeneous, porous coatings *ca.* 1 μm thick and with nanometric Ag particles as the main component. The presence of small amounts of Ag_2O was also inferred from XPS data. The reduction process of these films, which are used as electrodes over the potential range 3.0-0.0 V in lithium cells, consisted of several steps involving the formation of a solid electrolyte interface between 1.5 and 0.2 V, and at least two Ag-Li alloys below 0.2 V, the patterns of which were indexed in the cubic and tetragonal systems, respectively. The alloying/dealloying processes are reversible, and the cell can deliver a capacity of 600 Ah kg^{-1} in the potential window 1.0-0.0 V.
 [DOI: 10.1149/1.1632476]

Manuscript submitted February 10, 2003; revised manuscript received July 25, 2003. Available electronically December 9, 2003.

In the last few years, lithium-based alloys have aroused increasing interest as promising choices for use as negative electrodes in Li-ion batteries, particularly since the inception of the Stalion lithium-ion cell[1] developed by Fuji Photo Film Celltec. Co. (Japan), which showed that tin-based systems exhibit high specific capacities as anode materials by virtue of their ability to form Li_xSn alloys, $1.0 < x < 4.4$.

The reaction of these systems with lithium is well known and involves a decomposition step that yields Li_2O and Sn, followed by the formation of various Li-Sn alloys.[2-5] The decomposition reaction is electrochemically irreversible, so most of the initial discharge capacity cannot be recovered. Unfortunately, pure Sn tends not to react electrochemically with lithium. An alternative approach is to use tin-based intermetallic composites as electrodes in lithium cells. Good results have been obtained in this respect with Sn-Fe,[6] Cu-Sn,[7] Sn-Sb,[8] Ni-Sn,[9] and Sn-Ca[10] systems, where the elements accompanying tin act as inert matrices and help mitigate disintegration and mechanical failure of the electrode through the significant volume changes resulting from the formation of the Li_xSn alloy. Also, many researchers have focused on other elements capable of reversibly storing variable amounts of Li: Bi,[11] Mg,[12] Sb,[13] Si,[14] Zn,[15] and Pb.[16]

Silver is one other element capable of alloying with lithium to form $AgLi_x$ compounds ($x \approx 3.3$, theoretical capacity 827 Ah kg^{-1}[17]). Moreover, there is much experience in silver compounds used as electrodes in primary button cells, and the element can be easily obtained with simple conventional techniques, requiring no inert atmosphere. These advantageous features are attractive enough to test this element as an electrode material in rechargeable lithium cells. Silver has so far been used as a diluting matrix to retard the aggregation of tin in Sn[18] and Sn-Sb[19] electrodes. This communication explores the reactivity of silver films in lithium cells. Preliminary electrochemical tests exposed the potential of elemental Ag as an anodic material for electrochemical devices.

Experimental

A spray pyrolysis method was used to prepare the Ag coatings. Compressed atmospheric air was used to atomize a solution containing the precursor compound through a spray nozzle over the heated substrate.[20] The substrate holder was equipped with thermocouples and heating elements, the latter governed by a temperature controller. The substrate was moved forward and backward at a fixed frequency by an electronically controlled step motor. An aqueous solution of 0.05 M $Ag(CH_3COO)$ was used as precursor. The solution was pumped into the airstream in the spray nozzle at a rate of 50 mL h^{-1} with a syringe pump for a preset time of 20 min. An airstream of 25 L min^{-1} measured at 1.25 bar was used to atomize the solution. Circular disks 0.4 mm thick and of 7.5 mm diam of commercial 304 stainless steel were used as substrates. They were kept at temperatures over the range 225-300°C.

X-ray diffraction (XRD) patterns were recorded on a Siemens D5000 X-ray diffractometer, using Cu Kα radiation and a graphite monochromator, in steps of 0.02° and 1.2 s. Scanning electron microscopy (SEM) images were obtained on a Jeol JMS-5300 microscope. A Visiolog 5.2 software, from NOESIS, was used to characterize particle size by image processing. Thermogravimetric (TG) measurements were made on a CAHN 2000 thermobalance by heating from 25 to 600°C at a rate of 5°C min^{-1} under ambient conditions.

X-ray photoelectron spectroscopy (XPS) spectra were recorded on a Physical Electronics PHI 5700 spectrometer using nonmonochromated Mg Kα radiation and a hemispherical analyzer operating in the constant pass mode at 29.35 eV. Binding energies (BEs) were referred to the Ag $3d_{5/2}$ peak at 368.3 eV. Samples were mounted on a holder without adhesive tape and kept under high vacuum in the preparation chamber overnight before they were transferred to the analysis chamber of the spectrometer. Survey spectra over the range 0-1200 eV were recorded at a 187.85 pass energy, each region being scanned several times to ensure an adequate signal-to-noise ratio. A 3×3 mm sample area was sputtered by 4 keV Ar^+; the sputter rate was assumed to be $\sim$3 nm min^{-1}, as determined for Ta_2O_5 under identical sputtering conditions. Spectra were handled by PHI-Access V.6 and Multipak software, both from Physical Electronics. Curve fitting of high resolution spectra was carried out after Shirley background correction and satellite subtraction. The atomic concentration was determined from C 1s, O 1s, and Ag 3d peak areas, using Shirley background subtraction and sensitivity factors provided by the spectrometer manufacturer (Physical Electronics). An Ar^+ ion beam of 4 keV was used for depth profiling, the composition being determined from the integrated intensities of the XPS spectra.

Electrochemical experiments were carried out in two-electrode cells, using lithium as the anode. The electrolyte used was a Merck battery electrolyte LP 40, ethylene carbonate (EC):diethyl carbonate (DEC) = 1:1 w/w, 1 M $LiPF_6$). The stainless steel circular disks coated with the active material were used as working electrodes.

* Electrochemical Society Active Member.
z E-mail: iq2sagrl@uco.es

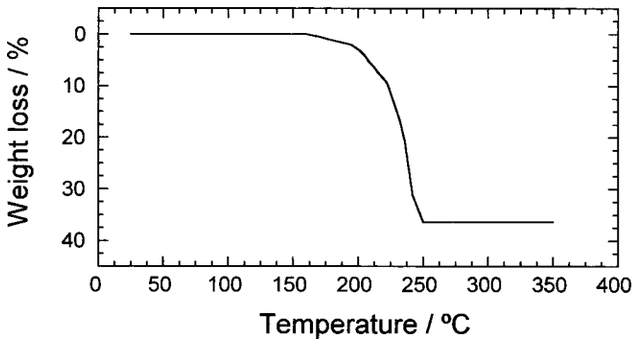

Figure 1. TG curve for silver acetate.

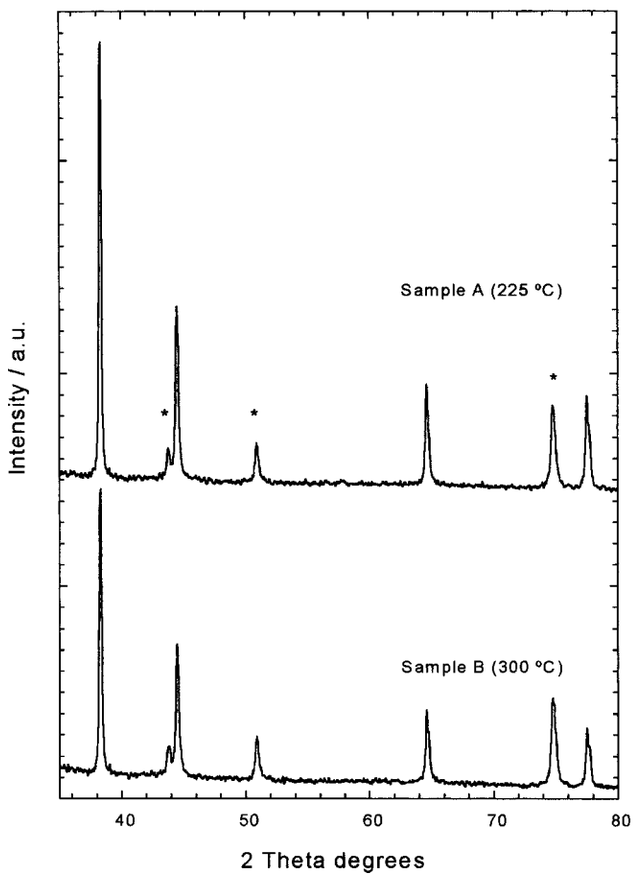

Figure 2. XRD patterns for the Ag thin film electrodes. (* are substrate reflections.)

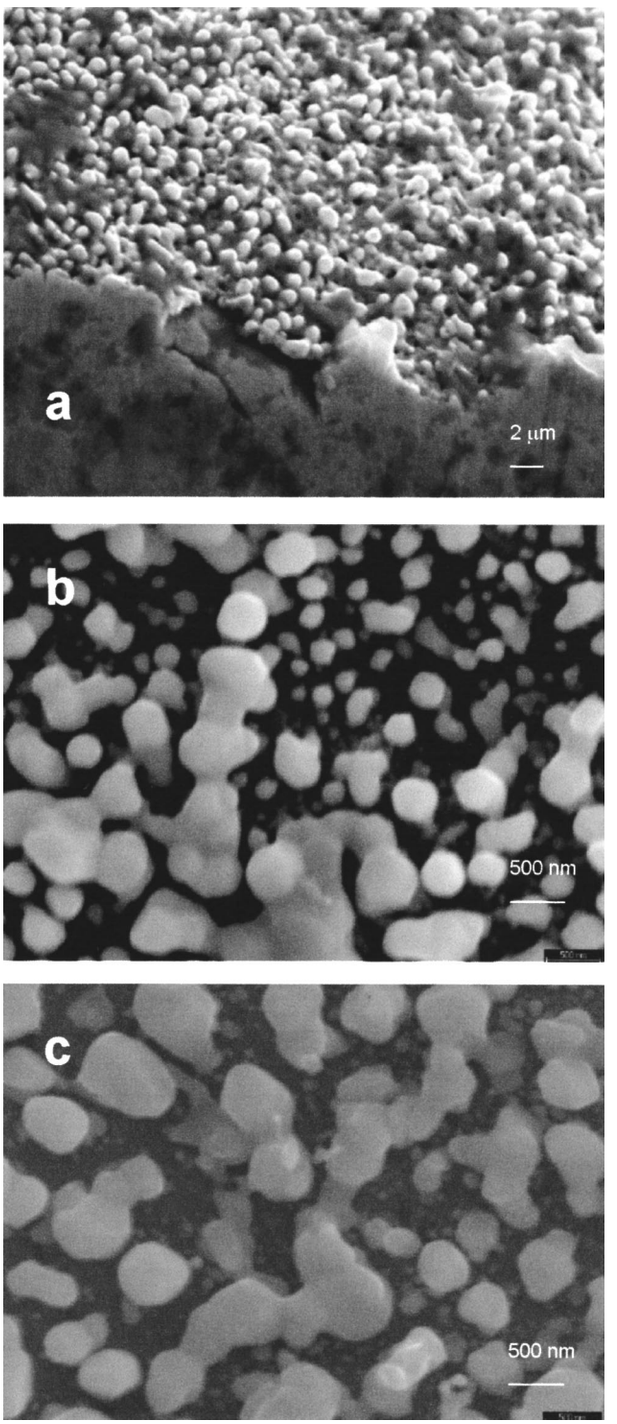

Figure 3. SEM images obtained for (a, b) sample A and (c) sample B.

Table I. Substrate temperature during precursor deposition, amount deposited (w), and structural parameters for the Ag thin film electrodes.

Compound	Temperature (°C)	w (mg cm^{-2})	a (Å)	L (nm)
Sample A	225	0.60	4.078_2	432
Sample B	300	0.20	4.078_2	593

Unless otherwise noted, a 0.05 mA mg^{-1} current density was applied to the cells for electrochemical measurements, controlled via a MacPile II potentiostat-galvanostat. Cyclic voltammetric tests were performed at a scan rate of 40 μV s^{-1}, using a Schlumberger SI-1286 potentiostat.

Results and Discussion

Two different coatings were prepared by heating the substrate at 225 and 300°C, resulting in samples A and B, respectively. These temperatures were chosen from TG measurements of

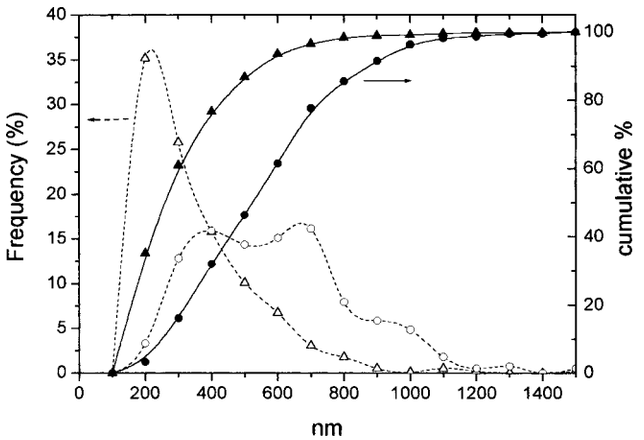

Figure 4. Particle size distribution of (△, ▲) sample A and (○, ●) sample B.

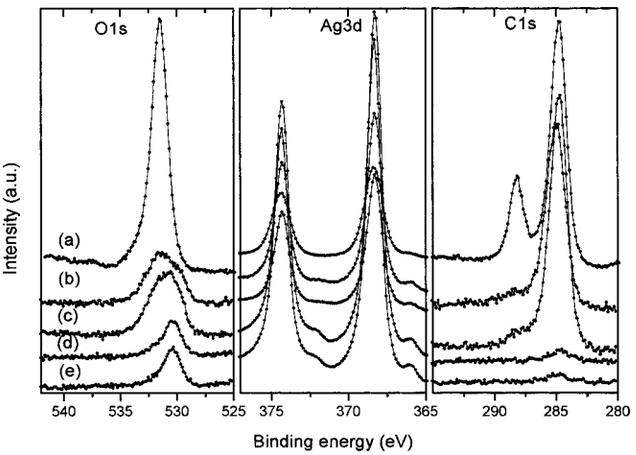

Figure 5. O 1s, Ag $3d_{5/2}$, and C 1s XPS spectra corresponding to (a) pure silver acetate, (b) sample A, (c) sample B, (d) sample A after 2 min of argon etching, and (e) sample B after 2 min of argon etching.

$Ag(CH_3COO)$, the weight loss of which fell within the previous temperature range (see Fig. 1). A short heating time (15 min) was used to obtain nanoparticle films of pure Ag (as inferred from the XRD patterns). Figure 2 shows the XRD patterns for the coatings, with the typical reflections for Ag. The remaining peaks were assigned to the substrate, and no additional peaks belonging to the undecomposed precursor were observed. The unit cell parameters, shown in Table I, are consistent with those reported for Ag. Crystallite sizes were obtained using the Scherrer equation[21] and are also included in Table I; they increased with increasing temperature. Moreover, the amount of material deposited decreased with increasing temperature, probably because a drop of the precursor solution burst and spilled part of its component off the substrate. This phenomenon has often been observed in the preparation of various oxides by spray pyrolysis.[22]

Figure 3 shows the SEM images obtained. Thorough coating of the substrate is apparent from the cross-sectional image obtained for sample A, from which the film thickness can be estimated to be around 1 μm. The silver grains tend to be round. Figure 4 shows the size frequencies (open symbols) and cumulative percentages (solid symbols) corresponding to the particle size distribution for the two samples. The particle size for sample A ranged from 300 to 500 nm; that for the sample sprayed at higher temperatures (sample B) ranged from 500 to 900 nm. These values are fairly consistent with those obtained from X-ray peak broadening (see Table I). Thus, the SEM images show that, when the sprayed solution is deposited on the heated substrate, the films consist of nanosized particles that form a highly porous framework. The smaller particle size of sample A must lead to a more compact film and hence to a higher apparent thin film density. One also observes an interconnected system of channels close to the steel surface that results from sintering of Ag particles as suggested by the XPS data discussed in the next paragraph. The coating is defined by this gel-like layer where quasi-spherical grains stand out, and the thickness is essentially dictated by the size of these round particles (Fig. 3a).

Figure 5 shows the XPS spectra for films subjected to various treatments. The XPS spectrum for silver acetate was also recorded for comparison. The C 1s XPS spectrum for pure silver acetate exhibits two peaks, one centered at 288.3 eV[23] and assigned to the carboxylate group, and the other at 284.8 eV and due to the methyl group. The increased area under the latter peak is a result of the additional contribution of adventitious carbon. The atomic compositions obtained (Table II) reveal a carbon content nearly twice as high as that in the nominal acetate stoichiometry. While this peak is maintained in the spectra for the films, the former virtually disappears (only a weak signal, nearly coincident with the background, is detected). This reveals that acetate decomposition is virtually complete at the two temperatures studied. This is also reflected in the O 1s emission spectrum, the intensity of which is significantly decreased (the atomic percentage is nearly one-half, Table II). Moreover, this peak becomes more asymmetric as discussed below. The value of the Ag $3d_{5/2}$ BE obtained for the acetate precursor and deposited silver is virtually the same, 384.4 eV, which makes it difficult to discriminate between Ag^0, as found by XRD, and Ag^+. Identifying the valence states of silver from the BE values is not easy because they are closely spaced. Thus, values for the BE of the Ag $3d_{5/2}$ photoemission between 368.1 and 368.4 eV have been reported for Ag, and values over the ranges 367.3-367.6 and 367.8-368.0 eV have been obtained for Ag_2O and AgO, respectively. Greater differences exist in the Auger Ag_{MNN} peak, which appears at 358.0, 350.6, and 355.5 eV on the kinetic energy scale for Ag, Ag_2O, and AgO, respectively.[23] The value obtained from the films, whichever the preparation temperature, is better explained by assuming the formation of metallic silver, a conclusion that is also consistent with the XRD data.

The O 1s peak for the films is complex, with many components corresponding to different chemical states. The peak profile was fitted to four components, as shown in Fig. 6. The peak near 532.0 eV (curve 1) can be assigned to hydroxyl or water species.[24,25] The second peak, centered at 531.6 eV (curve 2), could be assigned to traces of undecomposed silver acetate or an intermediate species that maintains a C—O bond (viz. CO_3^{2-}). The C 1s photoemission peak exhibits a reduced intensity peak at 288.15 eV, a value similar to that for the carboxyl group. However, the oxygen-to-carbon intensity ratios found in the film samples are greater than that for pure silver acetate, so this oxygen species is also bonded to other species. Atomic oxygen on a metallic silver surface and dissolved subsurface atomic oxygen have been shown to posses a BE near 531 eV[24,26] (curve 3). Finally, the peak at the highest energy (529.2 eV) can be assigned to oxygen forming Ag_2O rather than AgO, the O 1s peak for which appears at 528 eV.[23]

Table II. Atomic compositions obtained from XPS data.

Compound	C 1s (%)	O 1s (%)	Ag 3d (%)
$Ag(CH_3COO)$	58	26	16
Sample A	59	15	26
Sample B	64	12	24
Sample A (2 min Ar etching)	4	7	89
Sample B (2 min Ar etching)	5	7	88

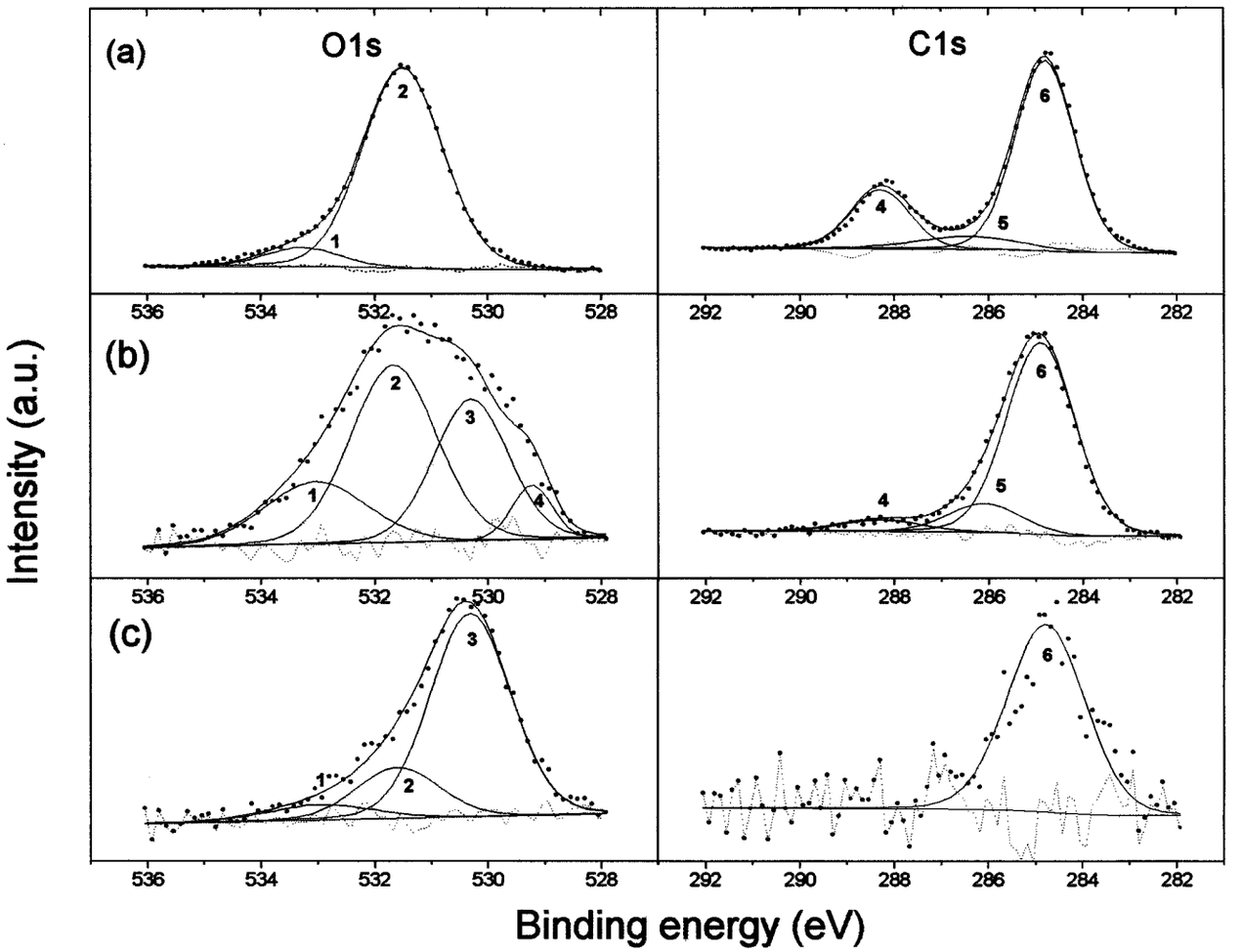

Figure 6. O 1s and C 1s peak curve fitting: (a) pure silver acetate, (b) sample A, and (c) sample A after 2 min of argon etching.

To shed additional light on the previous findings, films were sputtered with Ar^+ for 2 min. The XPS spectra for these samples are depicted in Fig. 5 and 6. The most salient changes were as follows. (*i*) The C 1s peak almost disappeared. The atomic concentration dropped to 4-5% (see Table II), which confirms its assignation to adventitious carbon. (*ii*) The O 1s peak was markedly weaker and more symmetric. The atomic percentage dropped to 7%, and only the peak centered at 529.0 eV (in our opinion associated to silver oxide) was detected. (*iii*) The Ag 3d photoemission remained highly symmetric, and its BE hardly shifted. From these results, the following conclusions can be drawn on the surface structure of the films: virtually complete decomposition of acetate is observed at the temperatures used; also, the C 1s peak obtained is due mainly to adventitious carbon. The main component of the films is metallic silver, which, based on the O 1s peak deconvolution, is accompanied by a small amount of Ag_2O. Direct identification from the Auger transition failed because no signal could be identified around 350 eV on the kinetic energy scale. The two oxidation states of silver are indistinguishable from the BE of the 3d photoemission peak. No peaks belonging to the main substrate components (Fe, Cr) were detected in this analysis. This means that silver is also the component of the black background of the SEM images previously described as an interconnected channel system.

The XPS concentration depth profiles for silver, iron, oxygen, and carbon are shown in Fig. 7. After a few minutes of etching, the oxygen concentration could not be measured. This suggests that the Ag_2O film was very thin, particularly for sample B (around 50 nm if we assume a depth of 10 nm per min of ion Ar^+ etching).[27] The O 1s peak disappeared after 5 min of etching; however, for sample A, such a peak continued to be detected after longer periods (more than 20 min). The silver concentration initially increased through removal of adventitious carbon and oxygen and then remained essentially constant up to 20 min of ion sputtering. Beyond that point, the silver concentration decreased gradually. The average rate of silver removal was lower for sample A, which is consistent with the larger amount deposited (see Table I). However, the thickness obtained from these depth profiles, 1-2 μm, is consistent with that inferred from the SEM images. Iron was detected after 20 min of sputtering, when the silver content started to decrease. These results suggest that the gel-like silver coating is very thin (<200 nm thick). When the silver content declines, the extracted silver comes from the grains. Except for the above-described subtle compositional divergences, no differences such as impurities or distinct phases in the samples were apparent from these depth profiles.

Figure 8 shows the first galvanostatic discharges performed on Li/Ag cells. While discharging, the potentials of the films rapidly drop to 1.5 V, which is followed by a negative slope to a cathode potential of 0.2 V and, finally, an extensive, nearly horizontal sequence up to 0.0 V. A subtle slope change is observed at 2.5 V which, based on XPS data, could be assigned to the reduction of Ag^+. The region between 1.5 and 0.2 V, which exhibits an almost linear decrease in potential with the faradaic yield, can be assigned to the formation of a solid electrolyte interface (SEI) film resulting from the reduction of electrolyte solvent, as reported for noble met-

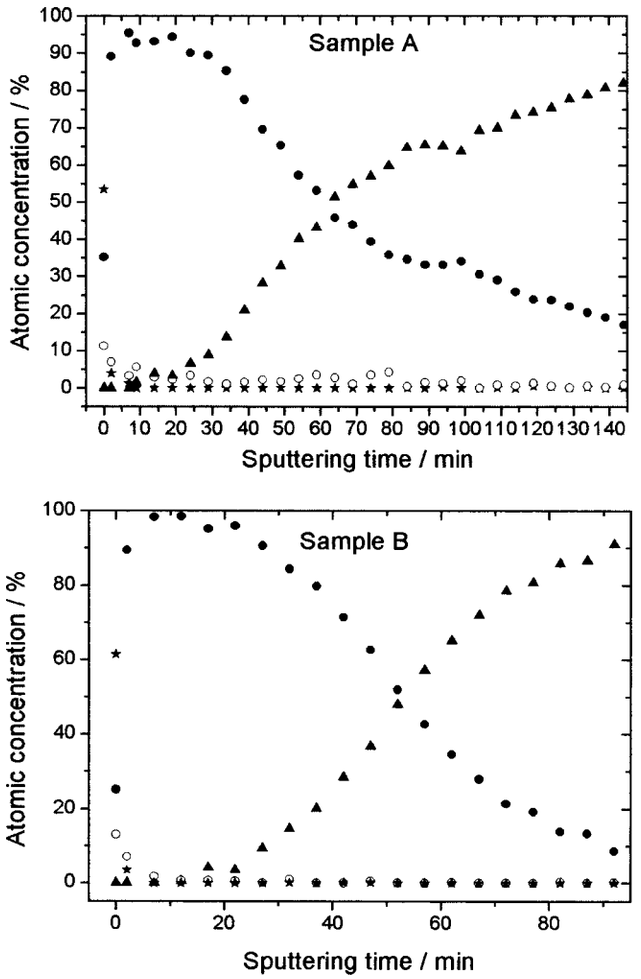

Figure 7. XPS depth profiles for (●) silver, (▲) iron, (○) oxygen, and carbon (⋆).

als used as electrodes in lithium batteries.[28,29] This phenomenon is more marked in sample B, which possesses a greater particle size and a smaller amount of active material. However, this behavior does not seem plausible, because the SEI filming reaction generally is dependent on the surface area and should be favored by an increased value of this parameter. The surface chemical state of the two samples may provide a more plausible explanation. Oxygen atoms, the content in which was somewhat higher in sample A (see Table II), are strongly bound to the surface of this sample, so their removal, as noted earlier, requires a more drastic treatment. This could afford more direct contact between the organic molecules of the electrolyte and silver atoms, thus facilitating the formation of the SEI film. When the potential scale is enlarged, two plateaus can be observed in the 0.2-0.0 V region that are ascribed to Li-Ag alloys.[30] These two steps in the reduction process can also be inferred from the cyclic voltammetric curve of Fig. 9, even though the reduction peaks (particularly that at the lower potential) are not completely resolved under the conditions used. The anodic scan is better defined, with two rather symmetric peaks at 0.12 and 0.32 V in the voltammogram. This cyclic voltammogram differs from that reported by Wachtler,[18] who found a third anodic peak at *ca.* 0.4 V.

To analyze the structural changes undergone by silver during the discharging and charging processes, *ex situ* XRD patterns were recorded at different discharge and charge potentials. At a discharge potential of 1.0 V (Fig. 10), the main difference of the pattern from that for the parent film was a decreased intensity in the peaks for silver; however, no new peaks were observed. This is consistent with the cathodic scan as the reduction peaks start to develop below this potential. Only partial silver amorphization can be inferred from the pattern. At 0.0 V, the diffractogram changes significantly: new lines appear, the spacings of which are shown in Table III. This set of lines, that of low intensity at 26.7° (2θ) excluded, can be indexed in a tetragonal system with the following cell parameters: $a = 5.41(1)$ and $c = 5.60(2)$ Å. Besides these lines, one can detect a set of reflections located at Bragg angles somewhat smaller than those for pure silver. These reflections can be indexed in a cubic system with $a = 4.042(3)$ Å (Table IV). Compared with silver (Table I), the unit cell has contracted. In our opinion, these data define a new Ag-Li alloy, probably with a small lithium content, rather than pure Ag. Thus, the reduction with lithium up to 0.0 V leads to the formation of at least two alloys, one tetragonal ($AgLi_y$) and the other cubic ($AgLi_x$). Unfortunately, it is very difficult to accurately determine their lithium contents from electrochemical measurements, as $x + y = 2.4$. None of these alloys coincides with those reported in the Joint Committee on Powder Diffraction Standards (JCPDS) files [AgLi (card no. 4-805) and Ag_3Li_{10} (card no. 2-1097)]. Differences in synthetic procedures may account for this discrepancy. When the cell is charged at 0.2 V, the intensity of the peaks close to the silver increases, and the unit cell dimension approaches that for pure Ag. This means that Li^+ is extruded from the $AgLi_x$ alloy and the Ag framework as a result. The similarity between the unit cells of both phases ($AgLi_x$ and Ag) results in slight polarization between the reduction and oxidation peak. Finally, when the cell is charged at 1.0 V, most of the peaks belonging to the tetragonal phase disappear (only the more intense reflections at 2.27 and 2.21 Å still remain, but with a reduced intensity), and Ag reflections are stronger. We can thus assign the oxidation peak at 0.32 V to the extrusion of Li from $AgLi_y$ and its conversion into metallic silver. The fact that the formation peak appears at 0.04 V (0.28 V below the corresponding decomposition peak) is indicative of the greater structural rearrangement required to transform the cubic phase into a tetragonal phase.

The performance of the Li/Ag cells was studied by analyzing the specific capacity delivered by the electrodes on cycling (Fig. 11). Thus, the Li/Ag cells were discharged up to 0.0 V and then cycled over the range 0.0-1.0 V. Good capacity retention was observed for sample A, which retained nearly 95% of its delivered capacity over the first 12 cycles (Fig. 11a). By contrast, the capacity retention of sample B faded rapidly. Additional information can be obtained by plotting the charge recovery, as the ratio between the specific capacity delivered in each charge process and the previous discharge process, against the number of cycles. For sample A, the charge recovery was close to 100%, which testifies to the good reversibility of the alloying/dealloying processes involved (Fig. 11b). Conversely, the cell made from sample B has a low charge recovery (Fig. 11b). The increased particle size, together with a greater ability to form SEI films, may be the origin of the poorer electrochemical response of this cell, the capacity of which fades after the first six cycles. Following prolonged cycling, the capacity of sample A also fades, and the cell delivers only 150 Ah kg^{-1} at the 50th cycle. This capacity drop can be explained in the light of (*i*) the volume changes resulting from alloying/dealloying processes and the subsequent stress and strain undergone by the active material, and (*ii*) the lack of a matrix that can partially mitigate the stress (a role played by Li_2O in tin composite electrodes). However, the capacity retention of the Ag electrode is substantially improved relative to other elements such as Bi,[11] Si,[31] or Sn[32] (95 *vs.* 30-50%); these advantages make Ag thin films potential candidates for use in Li-ion microbatteries. Additional efforts must be made to find an inert matrix that will allow the cycle life of silver thin electrodes to be extended.

Conclusions

Spray pyrolysis of aqueous silver acetate solutions is a simple, effective method for preparing silver thin films at moderate tempera-

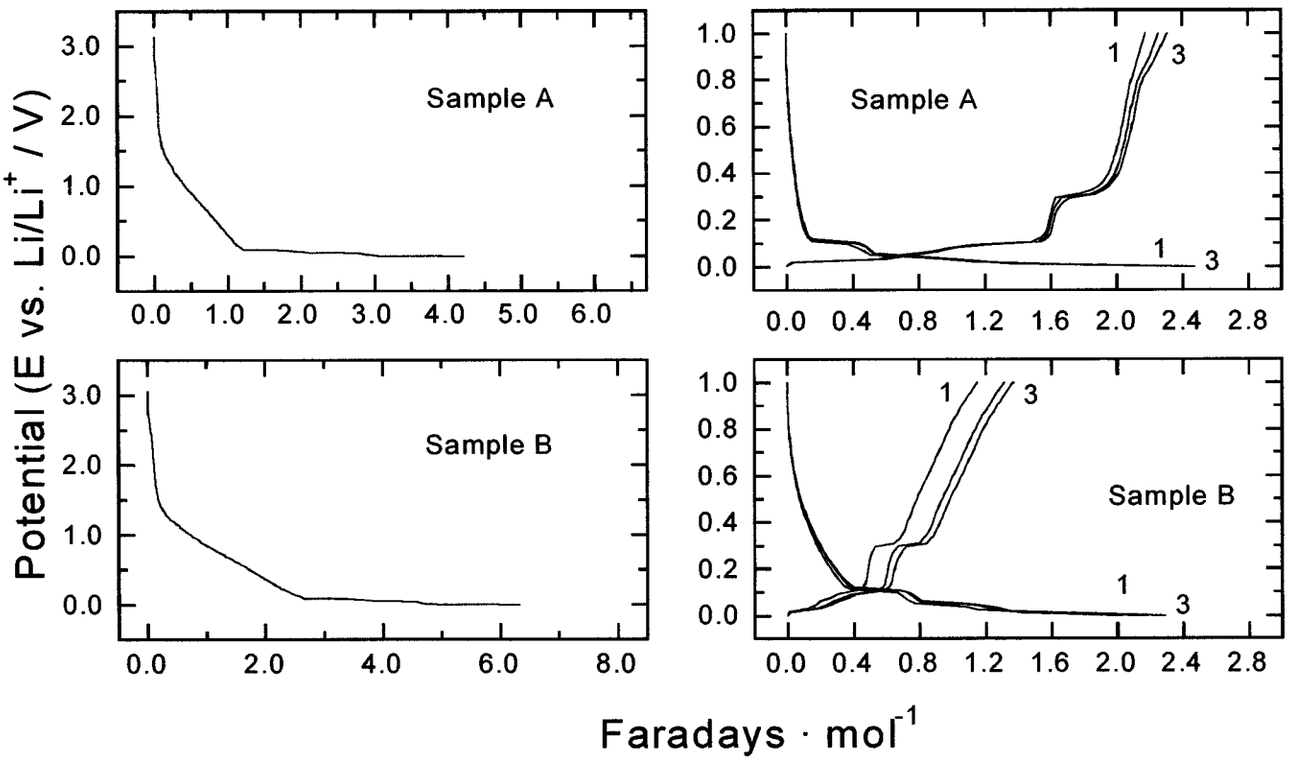

Figure 8. First-discharge and subsequent charge-discharge galvanostatic curves for Li/Ag cells.

tures. Above 200°C, the organic salt is virtually decomposed, and the substrate is thoroughly coated with a highly uniform, homogeneous film consisting of nanometric, spherical particles. Under these conditions, the sole crystalline phase detected in the film is Ag; however, XPS spectra reveal a more complex surface structure containing small amounts of oxidized species (probably Ag_2O). These thin films can react reversibly with lithium in a Li/$LiPF_6$, EC-DEC/ film cell configuration over the potential range 0.0-1.0 V and form various reversible Ag-Li alloys that can be identified by combining cyclic voltammetry with *ex situ* XRD measurements. The good capacity retention of the cell (particularly that made from the film with smaller particle size) together with the very low potential make these films attractive candidates as anodes for Li-ion microbatteries.

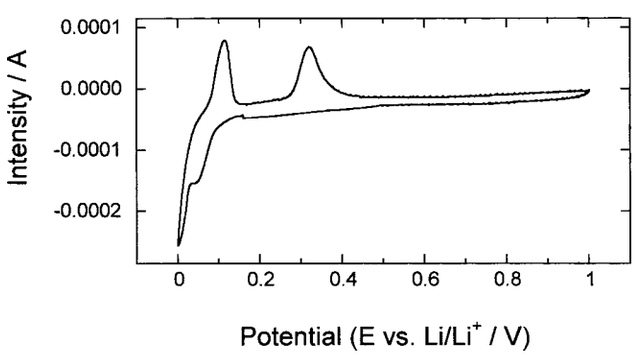

Figure 9. Cyclic voltammogram for a Li/sample A cell over the range 0.0-1.0 V.

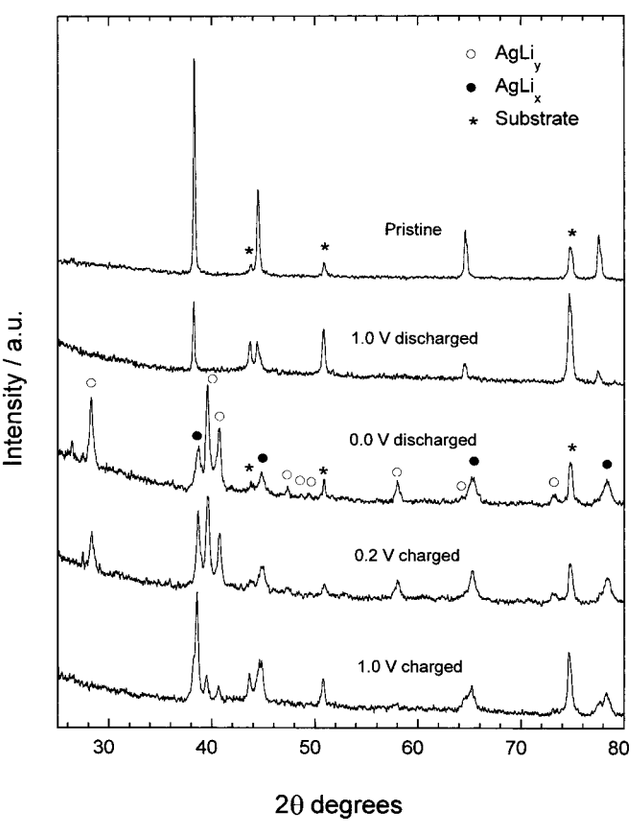

Figure 10. *Ex situ* XRD patterns recordered at different discharge (1.0 and 0.0 V) and charge (0.2 and 1.0 V) cutoff potentials for sample A.

Table III. Structural parameters assigned to the $AgLi_y$ phase.

	d (Å)	*hkl*
Lattice: tetragonal	3.1539	1 1 1
	2.2750	1 1 2
$a = b = 5.41(1)$ Å	2.2141	2 1 1
	1.9187	2 2 0
$c = 5.60(2)$ Å	1.8675	0 0 3
	1.8442	2 1 2
$\alpha = \beta = \gamma = 90°$	1.5886	2 2 2
	1.4484	3 2 1
	1.2907	3 0 3

Table IV. Structural parameters assigned to the $AgLi_x$ phase.

	d (Å)	*hkl*
Lattice: cubic	2.3253	1 1 1
$a = 4.042(3)$ Å	2.0214	2 0 0
$\alpha = 90°$	1.4288	2 2 0
	1.2197	3 1 1

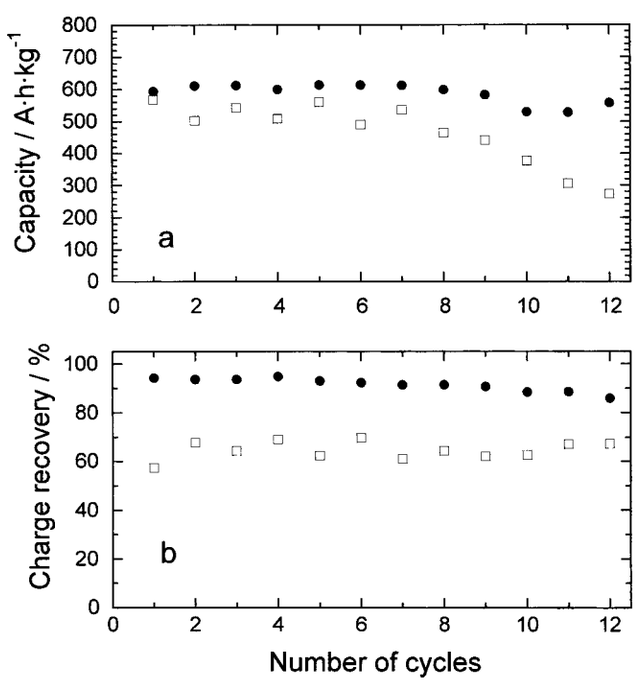

Figure 11. Delivered (a) specific capacity and (b) charge recovery on cycling for Li/Ag cells: (●) sample A, (□) sample B.

Acknowledgments

This work was supported by Junta de Andalucía (Group FQM-175) and Ministerio de Ciencia y Tecnología (Project MAT2002-04477-C02-02).

The University of Cordoba assisted in meeting the publication costs of this article.

References

1. Y. Idota, M. Mishima, M. Miyaki, T. Kubota, and T. Misayaka, Eur. Pat. Appl. 651450 A1 950503 (1995).
2. I. A. Courtney and J. R. Dahn, *J. Electrochem. Soc.*, **144**, 2045 (1997).
3. I. A. Courtney, W. R. McKinnon, and J. R. Dahn, *J. Electrochem. Soc.*, **146**, 59 (1999).
4. I. A. Courtney, R. A. Dunlap, and J. R. Dahn, *Electrochim. Acta*, **45**, 51 (1999).
5. J. Morales and L. Sánchez, *J. Electrochem. Soc.*, **146**, 1640 (1999).
6. O. Mao and J. R. Dahn, *J. Electrochem. Soc.*, **146**, 423 (1999).
7. K. D. Kepler, J. T. Vaughey, and M. M. Thackeray, *Electrochem. Solid-State Lett.*, **2**, 307 (1999).
8. J. Yang, Y. Takeda, N. Imanishi, and O. Yamamoto, *J. Electrochem. Soc.*, **146**, 4009 (1999).
9. G. M. Ehrlich, C. Durand, X. Chen, T. A. Hugener, F. Spiess, and S. L. Suib, *J. Electrochem. Soc.*, **147**, 886 (2000).
10. L. Fang and B. V. R. Chowdari, *J. Power Sources*, **97-98**, 181 (2001).
11. O. Crosnier, X. Devaux, T. Brousse, P. Fragnaud, and D. M. Schleich, *J. Power Sources*, **97-98**, 188 (2001).
12. Z. Shi, M. Liu, D. Naik, and J. L. Gole, *J. Power Sources*, **92**, 70 (2001).
13. X. B. Zhao, G. S. Cao, C. P. Lv, L. J. Zhang, S. H. Hu, T. J. Zhu, and B. C. Zhou, *J. Alloys Compd.*, **315**, 265 (2101).
14. H. Li, X. Huang, L. Chen, Z. Wu, and Y. Liang, *Electrochem. Solid-State Lett.*, **2**, 547 (1999).
15. Z. Shi, M. Liu, and J. L. Gole, *Electrochem. Solid-State Lett.*, **3**, 312 (2000).
16. M. Martos, J. Morales, L. Sánchez, R. Ayouchi, D. Leinen, F. Martín, and J. R. Ramos-Barrado, *Electrochim. Acta*, **46**, 2939 (2001).
17. JCPDS card no. 2-1097.
18. M. Wachtler, M. Winter, and J. O. Besenhard, *J. Power Sources*, **105**, 151 (2002).
19. M. Winter and J. O. Besenhard, *Electrochim. Acta*, **45**, 31 (1999).
20. R. Ayouchi, F. Martín, J. R. Ramos-Barrado, M. Martos, J. Morales, and L. Sánchez, *J. Power Sources*, **87**, 106 (2000).
21. H. P. Klug and L. E. Alexander, *X-Ray Diffraction Procedures for Polycrystalline and Amorphous Materials*, p. 665, John Wiley & Sons, New York (1974).
22. R. Ayouchi, F. Martín, D. Leinen, and J. R. Ramos-Barrado, *J. Cryst. Growth*, **246**, 191 (2002).
23. J. F. Moulder, W. F. Stickle, P. E. Sool, and K. D. Bomber, *Handbook of X-Ray Photoelectron Spectroscopy*, Perkin-Elmer, Eden Prairie, MN (1992).
24. G. N. Salaita, Z. F. Hazos, and G. B. Hoflund, *J. Electron Spectrosc. Relat. Phenom.*, **107**, 73 (2000).
25. V. I. Bukhtiyarov, M. Havecker, V. V. Kaichev, A. Knop-Gericke, R. W. Mayer, and R. Schlogl, *Nucl. Instrum. Methods Phys. Res. A*, **470**, 302 (2001).
26. A. I. Boronin, S. V. Koscheev, and G. M. Zhidomirov, *J. Electron Spectrosc. Relat. Phenom.*, **96**, 43 (1998).
27. E. György, A. Perez del Pino, P. Serra, and J. L. Morenza, *Surf. Coat. Technol.*, **173**, 265 (2003).
28. D. Aurbach, A. Zaban, Y. Ein-Ein, I. Weissman, O. Chusid, B. Markovsky, M. Levi, E. Levi, A. Schechter, and E. Granot, *J. Power Sources*, **68**, 91 (1997).
29. X. Wu, H. Li, L. Chen, and X. Huang, *Solid State Ionics*, **149**, 185 (2002).
30. S.-M. Hwang, H.-Y. Lee, S.-W. Jang, S.-M. Lee, S.-J. Lee, H.-K. Baik, and J.-Y. Lee, *Electrochem. Solid-State Lett.*, **4**, A-97 (2001).
31. S. Bourderau, T. Brousse, and D. M. Schleich, *J. Power Sources*, **81-82**, 233 (1999).
32. A. H. Whitehead, J. M. Elliot, and J. R. Owen, *J. Power Sources*, **81-82**, 33 (1999).